Thermomechanical Analysis of Vibrations of Silent Block

V. Szüle [1], B. Pere [2]

[1]University of Széchenyi István, Department of Applied Mechanics
Square Egyetem 1, 9026 Győr, Hungary
Phone: +36 96 503 400
e-mail: szule.veronika@sze.hu

[2]University of Széchenyi István, Department of Applied Mechanics
Square Egyetem 1, 9026 Győr, Hungary
Phone: +36 96 503 400

Abstract: Vehicle components made of rubber or rubber like polymers usually exhibit large deformations. Cyclic deformations may induce increasing in temperature in elastic materials. In this paper after the summary of the basic physical laws and the description of basement of continuummechanics, taking into account the Neo-Hooke material law, an example will be presented which allows to calculate strain- and temperature changes.

1. Introduction

Generally, the most frequently used structural materials are metals which have high strength and stiffness. However, there are many cases, when other important properties come to the fore as well as high deformation by elastic behavior, high viscosity namely good damping effect. The metals do not have these above mentioned properties, but the rubber does. The rubber- thanks to its elastic behavior is able to establish an elastic connection between hard and brittle structural elements, however, has high load carrying capacity.

Rubber can be classified as a so-called hyperelastic polymer which has a typical geometrical and material non-linear behavior. It means that the relationship between

displacements and internal forces can be described by functions whose order is higher than linear. The geometrical nonlinearity is easy to handle mathematically, however the material nonlinearity is only described approximately [1] [2]. Independent of the experimental investigations which deal with the material behavior of rubber, a number of theoretical works treated rubber as an ideally non-linear elastic, in particular hyperelastic material. One of the properties of the constitutive equations of hyperelastic material is that stresses are derived from stored elastic energy function. Hyperelasticity is a particularly convenient constitutive equation given its simplicity and it constitutes the basis for more complex material models such as elastoplasticity, viscoplasticity, and viscoelasticity [1].

Ogden [3] [4] was able to obtain very good correlation with the experiments of Treloar. Above that, his strain energy function fulfills all necessary mathematical and physical requirements. Furthermore, a number of material laws for rubber can be found in literature [5] [6] for example the Neo-Hooke-, the Mooney-Rivlin, the Yeoh-, and the Arruda-Boyce material models. Their applicapability largely depends on the stress.

Thus, description of the behaviour of rubber and rubberlike materials it is quite difficult from several aspects. The nonlinear behaviour and the fact that the strain can be comparable to the original measure of the parts shows that the models used for small strains cannot be applied even besides compromise.

Furthermore, the task becomes more complicated because of some features of rubber parts. The temperature of rubber increases significantly. Therefore, the temperature- and displacement fields are coupled, and it means that special solving algorithms are required [7]. So the equations of mechanics and thermodynamics are coupled.

As described above, the goals of this paper are the following:

It is necessary to summarize the applied equations and the basic physical laws which are responsible for the theoretical background [8]. Clarification of these relationships is essential because the material laws of rubber cannot violate those basic physical laws. It is necessary to extend these relationships like equilibrium of linear momentum and equilibrium of angular momentum, the first and second law of thermodynamics to high deformation of rubber and rubberlike polymers. After it, it will follow the numerical solution and computer simulation of the thermomechanical problem by using of the Neo-Hooke material law.

2. Notation

Table 1. Notation

Mechanics:	
$\vec{t}$	Force per unit surface/traction, acting on the material body
$\vec{f}$	Force per unit volume, acting on the material body
$\underline{\underline{\sigma}}$	Cauchy-stress tensor
$\vec{v}$	Velocity of the material body
ρ	Mass density
Continuum mechanics	
$\underline{\underline{F}}$	Deformation gradient tensor
$\vec{r}$	Position vector
J	Volume ratio
Thermodynamics	
ε	Energy supply density
$\vec{q}$	Heat flow vector
h	Heat source
η	Entropy density
φ	Free energy
φ_0	Free energy at the reference temperature
$\hat{c}$	Specific heat
Vector calculus	
$\vec{a} \cdot \vec{b}$	Scalar product (dot product) of two vectors
$\vec{a} \times \vec{b}$	Vector product (cross product) of two vectors
∇	Nabla, Hamiltonian differential operator

3. Basics of continuum mechanics

Consider a fixed reference configuration of a body corresponding to a fixed reference time t_0. The position of a typical point may be identified by the position vector $\vec{R}$. The reference configuration is assumed to be stress-free and possesses a homogeneous reference temperature value $T_0 (> 0)$.

Furthermore the quantities of the t_0 moment will indicated by capital letters and the quantities of an optional t moment will indicated by small letters. Thus, the position vector of material particle is $\vec{r}$ at time t. The position of the body is called current configuration at time t where each quantity depends on time. During the reference configuration the quantities do not depend on time, because of the fixed time moment. A map of the reference configuration to a current configuration is characterized by the macroscopic motion $\vec{r}(t) = \vec{\chi}(\vec{R}, t)$ [8].
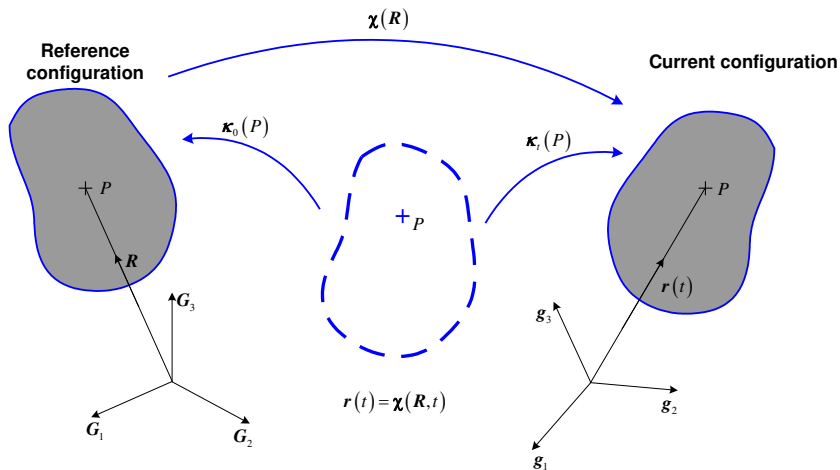

Figure 1. Connection between the reference and current configuration

Fig. 1 shows the connection between the reference and current configuration, i.e. movement and deformation of the body is determined by the $\vec{r}(t) = \vec{\chi}(\vec{R}, t)$ maping, so the P point which was originally determined by the $\vec{R}$ position vector moves to

the place determined by the $\vec{r}$ position vector. As a measure of the thermoelastic deformation we use the deformation gradient $\underline{\underline{F}} = grad\,\vec{\chi} = \dfrac{\partial \vec{\chi}(\vec{R})}{\partial \vec{R}} = \vec{\chi}(\vec{R}) \circ \nabla_0$, where the zero index of the differential operator ∇_0 means that the derivation has to be done in the reference configuration. Deformation gradient is the base variable of the continuum mechanical task and by using it the other quantities of the problem can be derived.

4. Governing equations

4.1. Equlibrium of linear momentum

Let us consider a hyperelastic continuum body in the current configuration. Its volume is indicated by v, and its surface is indicated by a. The integral formulation of equlibrium of linear momentum in the current configuration is:

$$\frac{d}{dt}\int_{(v)} \vec{v}\rho\,dv = \int_{(a)} \vec{t}\,da + \int_{(v)} \vec{f}\,dv \tag{1}$$

where $\vec{v}$ is the velocity of one point of the continuum body, ρ is the mass density of the material of the body, $\vec{t}$ force per unit surface/traction, $\vec{f}$ force per unit volume.

During the solution of the problem we need to know the differential formulation of the equlibrium of linear momentum, which can be generated by the Gauss's theorem:

$$\rho\dot{\vec{v}} = \underline{\underline{\sigma}} \cdot \nabla + \vec{f} \tag{2}$$

where $\vec{v}$ is the velocity of one point of the continuum body, ρ is the mass density of the material of the body, $\vec{t}$ force per unit surface, $\vec{f}$ force per unit volume, $\underline{\underline{\sigma}}$ Cauchy-stress tensor, namely the $\vec{t}$ traction can be expressed by the Cauchy-stress as follows: $\vec{t} = \underline{\underline{\sigma}} \cdot \vec{n}$.

4.2. Equilibrium of angular momentum

Let us consider a hyperelastic continuum body in the current configuration, its volume is indicated by v, and its surface is indicated by a. The integral formulation of equilibrium of angular momentum in the current configuration is:

$$\frac{d}{dt} \int_{(v)} \vec{r} \times \vec{v} \rho \, dv = \int_{(a)} \vec{r} \times \vec{t} \, da + \int_{(v)} \vec{r} \times \vec{f} \, dv \tag{3}$$

Hereafter, we use the differential form of the equilibrium of angular momentum in the current configuration:

$$\vec{r} \times \left(\rho \dot{\vec{v}} - \underline{\underline{\sigma}} \cdot \nabla - \vec{f} \right) = \overset{\downarrow}{\vec{r}} \times \underline{\underline{\sigma}} \cdot \nabla \tag{4}$$

The differential form of the balance of moments can be expressed by the following equality $\underline{\underline{\sigma}} = \underline{\underline{\sigma}}^T$. The consequence of this formula is that the stress tensor is symmetric.

4.3. The first law of thermodynamics

Cyclic finite deformations cause exoterm process in hyperelastic materials. The classical thermodynamical characterization of the continuum body is presented by Holzapfel and Simo [8], where the laws of thermodynamics, the Helmholtz free energy and the heat conduction play a significant role.

The form of the first law of thermodynamics in the current configuration is:

$$\frac{d}{dt} \int_{(v)} \dot{\varepsilon} \rho \, dv = -\int_{(a)} \vec{q} \cdot \vec{n} \, da \ + \int_{(v)} h \, dv + \underbrace{\int_{(a)} \vec{v} \cdot \vec{t} \, da}_{\text{Performance of forces on surface}} + \underbrace{\int_{(v)} \vec{v} \cdot \vec{f} \, dv}_{\text{Performance of forces on volume}}$$

$$\tag{5}$$

where ε is the energy density (energy per unit mass), $\vec{q}$ is the heat flux, h is the heat source.

Using Gauss's theorem the differential form of the Eq. (5) is:

$$\dot{\varepsilon}\rho = \left[-\nabla \cdot \vec{q} + h\right] + \left[\underline{\underline{\sigma}} \cdot \underline{\underline{l}} + \rho \vec{v} \cdot \dot{\vec{v}}\right] \tag{6}$$

where $\vec{v} \cdot \dot{\vec{v}} = \dfrac{d}{dt}\left(\dfrac{v^2}{2}\right)$, $\dfrac{d}{dt}\left(\varepsilon - \dfrac{v^2}{2}\right)\rho = \left[-\nabla \cdot \vec{q} + h\right] + \underline{\underline{\sigma}} \cdot \underline{\underline{l}}$, $\underline{\underline{l}} = \vec{v} \circ \nabla$ is the velocity

gradient, $\underline{\underline{l}} = \underline{\underline{\dot{F}}} \cdot \underline{\underline{F}}^{-1}$. Introducing the internal energy per unit mass $e = \varepsilon - \dfrac{v^2}{2}$ the

first law of thermodynamics in the current configuration has the following form:

$$\dot{e}\rho = \left[-\nabla \cdot \vec{q} + h\right] + \underline{\underline{\sigma}} \cdot \underline{\underline{l}} \tag{7}$$

4.4. The second law of thermodynamics

The behaviour of viscoelastic materials is described by the second law of thermodynamics. If the material is viscous and does stress-relaxing which is caused by stress, it can happen only in one direction. The stress decreases or increases. The status of an isolated system is proceeding to the thermal equilibrium.
The second law of thermodynamics can be expressed by the following inequality:

$$\frac{d}{dt}\int_{(v)} \eta\rho\,dv \geq -\int_{(a)} \frac{\vec{q} \cdot d\vec{a}}{T} + \int_{(v)} \frac{h\,dv}{T} \tag{8}$$

where η is the entropy density, T is the absolute temperature.

Using Gauss's theorem and the $\nabla \cdot \left(\dfrac{a}{b}\right) = \dfrac{\nabla \cdot a}{b} - \dfrac{a \cdot \nabla b}{b^2}$ identity the differential form

of Eq. (8) is:

$$\dot{\eta}T\rho \geq -\nabla \cdot q + \frac{q \cdot \nabla T}{T} + h \tag{9}$$

It will be expedient to change the variable of the exercise from entropy to temperature by applying the Legendre-transformation and by using the Helmholtz free energy

$$\psi = e - \eta T \tag{10}$$

Substituting Eq. (10) into Eq. (7) and subtract Eq. (7) from Eq. (10) the following expression is generated:

$$-\left(\dot{\psi}+\eta\dot{T}\right)\rho+\underline{\underline{\sigma}}\cdot\cdot\underline{\underline{l}}-\frac{q\cdot\nabla T}{T}\geq 0, \tag{11}$$

this is the Clausius-Duhem inequality [6].

5. Constitutive model

5.1. Stress state of elastic element

The property of an elastic element is that the total mechanical energy is reversible. The free energy of the body is the function of the strain and temperature. Dissipation comes only from heat conduction.

5.2. Structure of free energy function

In order to make the further calculations easier it is necessary to split the Eq. (10) to temperature-dependent and temperature-independent parts [12]. Based on known functions $\tilde{\psi}_0\left(\underline{\underline{C}}\right)$ and $e_0\left(\underline{\underline{C}}\right)$ for the free energy and the internal energy at a given reference temperature T_0 and the given heat capacity $\hat{c}$ at a reference temperature, one obtains the following general structure for the thermoelastic free energy from the Eq. (10):

$$\psi\left(\underline{\underline{C}},T\right)=\tilde{\psi}\left(\underline{\underline{C}},\tilde{T}\right)=\frac{T}{T_0}\psi_0\left(\underline{\underline{C}}\right)+(1-\frac{T}{T_0})e_0(J)+\int_{T_0}^{T}\hat{c}\left(\underline{\underline{C}},\tilde{T}\right)\left(1-\frac{T}{\tilde{T}}\right)d\tilde{T}, \tag{12}$$

where $\underline{\underline{C}}$ is the right Cauchy-Green strain tensor [12].

5.3. Neo-Hooke material law

In the following section we are going to investigate the isotrop materials and we are going to apply the Neo-Hookean material law. It means that ψ_0 which is used in free energy depends on the scalar invariant of the right Cauchy-Green strain tensor. The internal energy is zero applying the entropic theory and the c heat capacity is constant with good approximation. In the case of Neo-Hooke material the free energy is:

$$\psi\left(\underline{\underline{C}},T\right)=\tilde{\psi}\left(\underline{\underline{C}},\tilde{T}\right)=\frac{T}{T_0}\psi_0\left(\underline{\underline{C}}\right)+(1-\frac{T}{T_0})e_0(J)+\int_{T_0}^{T}\hat{c}\left(\underline{\underline{C}},\tilde{T}\right)\left(1-\frac{T}{\tilde{T}}\right)d\tilde{T}, \tag{13}$$

where

μ is the shear modulus,

C_I is the first scalar invariant of the right Cauchy-Green strain tensor, $C_I = \underline{\underline{C}} \cdot\cdot \underline{\underline{I}}$ [2].

5.4. Equation of heat conduction

Starting from the first law of thermodynamics and introducing the internal energy and changing the variable from entropy to temperature, the equation will have the next form:

$$\rho_0 c \dot{T} = \left(\underline{\underline{S}} - \rho_0 \frac{\partial \psi}{\partial \underline{\underline{C}}} \right) \cdot\cdot \frac{1}{2} \dot{\underline{\underline{C}}} + \rho_0 \frac{\partial^2 \psi}{\partial T \partial \underline{\underline{C}}} \cdot\cdot \dot{\underline{\underline{C}}} T - q_0 \nabla_0 + h_0 , \qquad (14)$$

where $\left(\underline{\underline{S}} - \rho_0 \dfrac{\partial \psi}{\partial \underline{\underline{C}}} \right) \cdot\cdot \dfrac{1}{2} \dot{\underline{\underline{C}}}$ is the non-recoverable part of the mechanical power,

which is zero in the case of a pure elastic element [1], [2]. In this case the reological model is regarded to be a pure elastic element. So the free energy of the body is characterized by the deformation and temperature:

$$\psi = \psi\left(\underline{\underline{C}}, T \right) \text{ or } \left(\underline{\underline{S}} - \rho_0 \frac{\partial \psi}{\partial \underline{\underline{C}}} \right) \cdot\cdot \frac{1}{2} \dot{\underline{\underline{C}}} = 0 , \text{ így } \underline{\underline{S}} = \rho_0 \frac{\partial \psi}{\partial \underline{\underline{C}}} \qquad (15)$$

Furthermore, we are assuming that there are not heat sources in the rubber and the temperature field shows homogeneous distribution. $h_0 = 0, q_0 = 0$

Thus, the equation of the heat conduction is the following:

$$c \dot{T} = T \frac{\partial^2 \psi}{\partial T \partial \underline{\underline{C}}} \cdot\cdot \dot{\underline{\underline{C}}} \qquad (16)$$

6. Example

Let us consider the mechanical model of a silent block, thus the A, B, C axisymmetric bodies (see Fig.2). The A and C bodies are rigid bodies, and B is a deformable one. Regarding the structure of the silent block it consists of two metal elements whose are connected by the rubber which is vulcanized between them. The

inside rubber part provides a non-linear elastic connection between the two metal elements in the following way: it transfers loads however filters out the harmful vibrations, i.e. it has damping effect. All three bodies are axysymmetric and their symmetry axes are the same.
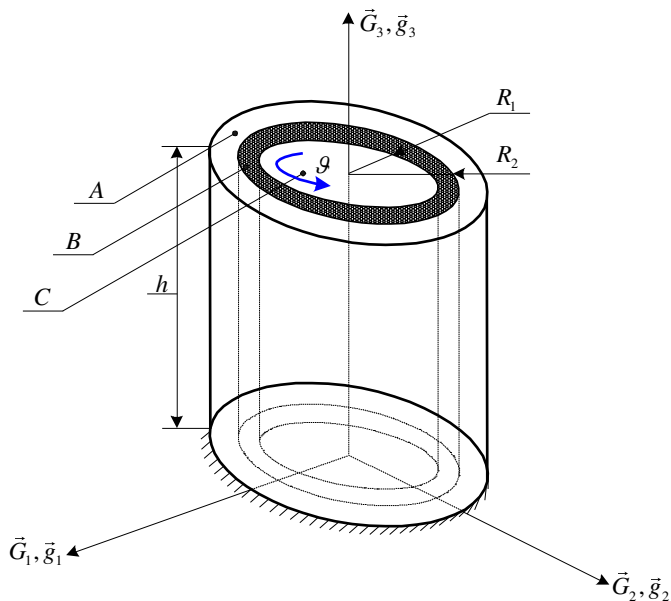

Figure 2. Mechanical modell of a silent block

The external body (A) is fixed and the internal one is imposed by a given rotation.

Further assumptions:

Planes perpendicular to the symmetric axis will be planes after the deformation.

The magnitude of the displacement is linear function of the measured distance from the axes of symmetry.

Furthermore, we are assuming that there aren't heat sources in the rubber and the temperature field shows homogeneous distribution, $h_0 = 0, q_0 = 0$.

We used the next material properties: $\mu = 4,225 \cdot 10^5 \left[\dfrac{N}{m^2} \right]$, c=1580 $\left[\dfrac{Nm}{kgK} \right]$.

Rotating the body C by angle ϑ , we have assigned the displacement of a point in body B on an optional radius, Fig. 3 and we have determined the relationship

between the reference and current configuration. Function $\vec{\bar{\chi}}\left(\vec{R},t\right)$ describing strain and characterizing the connection between the reference and current configuration has the following form on an optional radius:

$$
\left.\begin{array}{l}
x = \left(\cos\varphi\right)X + \left(\sin\varphi\right)Y, \\
y = \left(-\sin\varphi\right)X + \left(\cos\varphi\right)Y, \\
z = Z
\end{array}\right\} \vec{r}\left(t\right) = \vec{\bar{\chi}}\left(\vec{R},t\right),
\tag{17}
$$

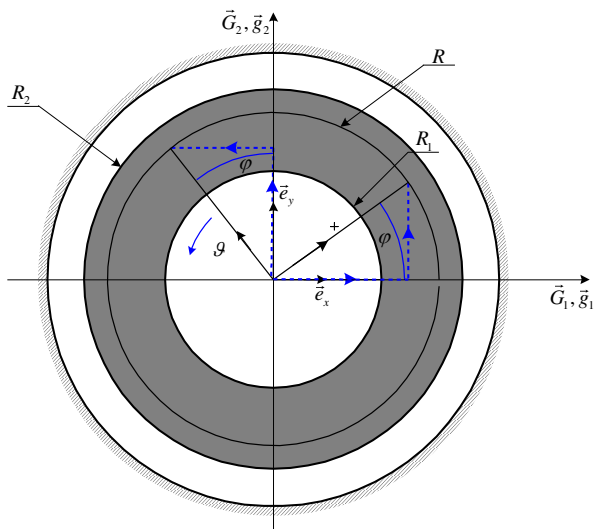where $\varphi = \vartheta\dfrac{R_2 - R}{R_2 - R_1}$, $R = \sqrt{x^2 + y^2}$.

Figure 3. Plan view of the mechanical model of the silent block

The deformation gradient is obtained by the derivation of the function $\vec{\bar{\chi}}\left(\vec{R},t\right)$.

Using this formula the problem of continuummechanics is regarded to be solved. Using of the deformation gradient we can derive the other quantities. We are assuming that the volume is constant so the deformation gradient can be expressed by the following way:

$$
\underline{\underline{F}} = \vec{\bar{\chi}}\left(\vec{R}\right) \circ \nabla_0 ,
\tag{18}
$$

Applying the Eq. (20) the Cauchy stress tensor is:

$$\underline{\underline{\sigma}} = \mu J^{-\frac{5}{3}} \left(\underline{\underline{b}} - \frac{1}{3} b_I \underline{\underline{I}} \right) + p\underline{\underline{I}} \,, \tag{19}$$

where μ is the shear modulus, $\underline{\underline{b}} = \underline{\underline{F}} \cdot \underline{\underline{F}}^T$ is the left Cauchy-Green strain tensor, b_I is the first scalar invariant of the left Cauchy-Green strain tensor, $J = \det\left(\underline{\underline{F}}\right) = 1$, $\underline{\underline{I}}$ is the identity tensor, p is the pressure, which is the consequence of the constant volume, it can be determined by the boundary conditions, in this case by the condition $\sigma_z = 0$.

After the substitution of the pressure p the Cauchy-stress tensor is obtained in the next formulation:

$$\underline{\underline{\sigma}} = \begin{bmatrix} \sigma_R & \tau_{R\varphi} & 0 \\ \tau_{\varphi R} & \sigma_{\varphi} & 0 \\ 0 & 0 & 0 \end{bmatrix}, \tag{20}$$

The calculation of the stress values is determined by program wxMaxima, and using of Eq. (20).

The stress σ_R is presented as the function of radius Fig. 4 and is compared with the simulation of the Ansys Finite Element Program. Results of both methods are in agreement with regard to their magnitude. One curve illustrates the changing of the values of stresses on the different radius of intermediate body B.
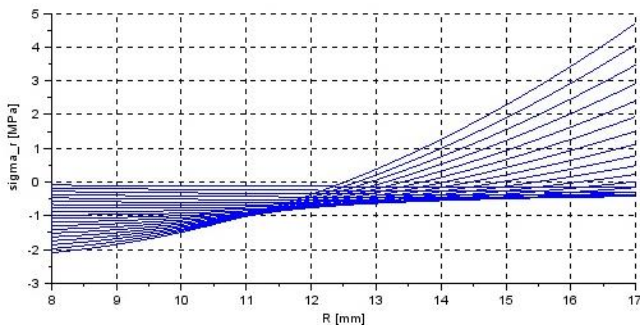

Figure 4. Representation of stress σ_R as the function of radius

The results of Fig. 4 illustrates very well the non-linear characterization of rubber's behaviour. Namely, decreasing or increasing of stress derives from the non-linear characterization.

Fig. 5 shows the result of the calculation by Ansys Finite Element Program.
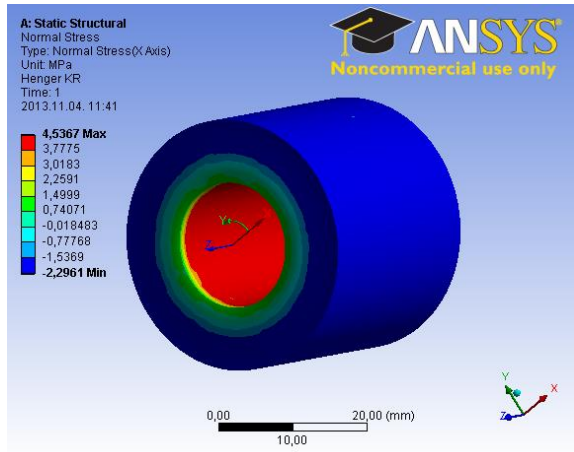

Figure 5. Representation of stress σ_R as the function of radius

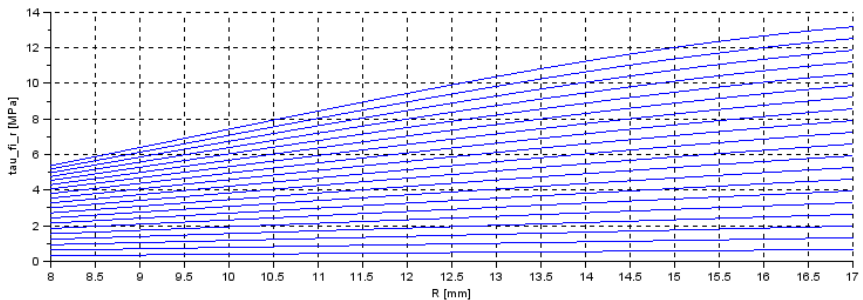*Figure 6. Representation of stress $\tau_{\varphi R}$ as the function of radius*

The same values were calculated by in the cases of the stresses σ_φ and $\tau_{\varphi R}$, like the same manner by using wxMaxima program and Scilab. The stress σ_φ is presented as the function of radius Fig. 7. One curve illustrates the changing of the values of stresses on the different radius of intermediate body B.
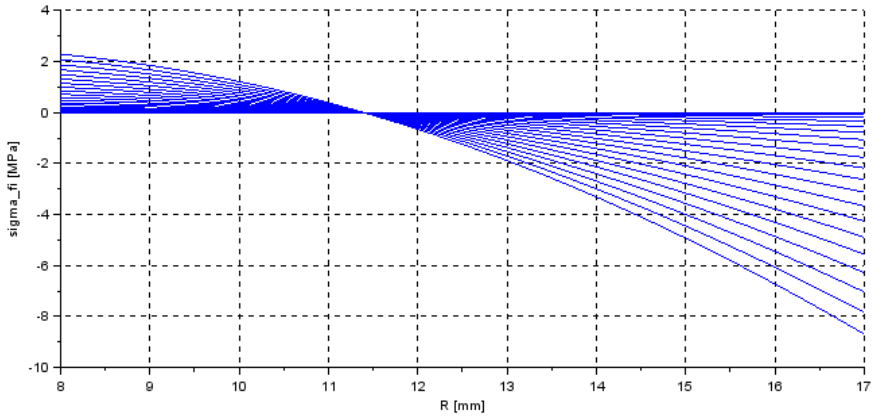
Figure 7. Representation of stress σ_φ as the function of radius

The Fig.7 shows the results of calculation by Scilab. Hence, this figure illustrates the changing of the stress σ_φ from radius R_1 to radius R_2 by the effect of the torsion of the internal body C from angle 0 to angle 10.

Fig.8 presents the temperature change by the effect of vibration frequency 1 Hertz.
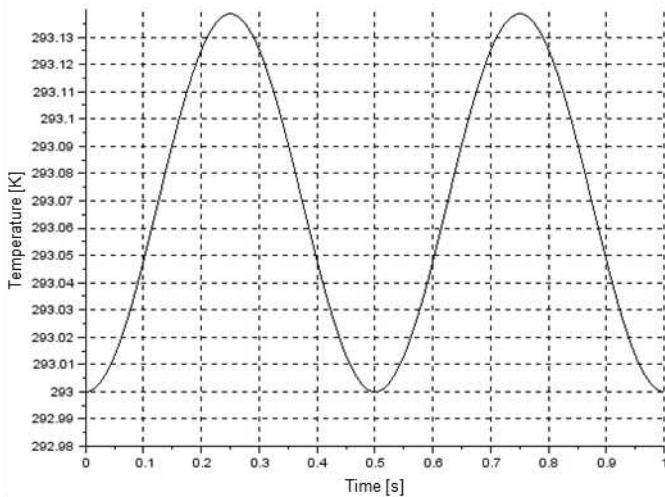

Figure 8. Temperature change as the function of time

The calculation of temperature changes which is caused by the effect of vibration frequency 1 Hertz is obtained by the using of Eq.(16), i.e. $c\dot{T} = T\dfrac{\partial^2 \psi}{\partial T \partial \underline{\underline{C}}} \cdot\cdot \dot{\underline{\underline{C}}}$.

Substitution of the next relation to the Eq.(16), $\varphi = \vartheta \sin\left(\omega t\right)\dfrac{R_2 - R}{R_2 - R_1}$ the temperature changes can be calculated. Generation of calculations and the representation of the temperature changes as the function of time were determined by the SCILAB program.

Summary

We represented an algorythm which allows to calculate strain changes and temperature changes of the rubber part of the silent block under certain conditions. In the future we would like to develop a solving computer program in order to apply it as a thermodinamically consistent description.

References

[1] J. Bonet, R. D. Wood, Nonlinear Continuum Mechanics for Finite Element Analysis, Cambridge University Press, 1997.

[2] G. A. Holzapfel, Nonlinear Solid Mechanics, John Wiley&Sons, Chichester, 2000.

[3] R. W. Ogden, Large deformation isotropic elasticity: on the correlation of theory and experiment for incompressible rubberlike solids, Proceedings of the Royal Society A 326 (1567) (1972) pp. 565-584.
doi: 10.1098/rspa.1972.0026

[4] R. W. Ogden, Large deformation isotropic elasticity: on the correlation of theory and experiment for incompressible rubberlike solids, Proceedings of the Royal Society A 328 (1575) (1972) pp. 567-583.
doi: 10.1098/rspa.1972.0096

[5] S. Reese, P. Wriggers, A material model for rubber-like polymers exhibiting plastic deformation: computational aspects and a comparison with experimental results, Computer Methods in Applied Mechanics and Engineering 148 (3-4) (1997), pp. 279-298.
doi: 10.1016/S0045-7825(97)00034-0

[6]   M. Böl, S. Reese, Finite element modelling of rubber-like polymers based on chain statistics, International Journal of Solids and Structures 43 (1) (2006) pp. 2-26.
doi: 10.1016/j.ijsolstr.2005.06.086

[7]   B. Pere, Solution of Coupled Thermomechanical Problems Using p-FEM, 8th European Solid Mechanics Conference (ESMC2012), Graz, Austria, 9-13 July 2012 (CD-ROM, 2 pages)

[8]   G. A. Holzapfel, J. C. Simo: Entropy elasticity of isotropic rubber-like solids at finite strains, Computer Methods in Applied Mechanics and Engineering 132 (1-2) (1996), pp. 17-44.
doi: 10.1016/0045-7825(96)01001-8

[9]   P. J. Flory, Statistical Mechanics of Chain Molecules, reprinted edition, Oxford University Press, New York, 1989.

[10] L.R.G. Treloar, The Physics of Rubber Elasticity, 3rd Edition, Oxford University Press, New York, 1975.

[11] S.C.H. Lu, K. S. Pister, Decomposition of deformation and representation of the free energy function for isotropic thermoelastic solids, International Journal of Solids and Structures 11 (7-8) (1975) pp. 927-934.
doi: 10.1016/0020-7683(75)90015-3

[12] C. Miehe, Entropic thermoelasticity at finite strains. Aspects of formulation and numerical implementation, Computer Methods in Applied Mechanics and Engineering 120 (3-4) (1995) pp. 243-269.
doi: 10.1016/0045-7825(94)00057-T

Series of Experiments with Thermal Insulation Coatings Consisted of Vacuum-Hollow Nano-Ceramic Microspheres

D. Bozsaky[1]

[1]Széchenyi István University, Department of Architecture and Building Construction
Egyetem tér 1, H-9026 Győr, Hungaryy
Phone: +36 96 503 454
e-mail: bozsaky@gmail.com

Abstract: Because of the rigorous regulations in the 21st century it has become a serious task for designers to find more effective ways for thermal insulation. One of these options is the application of nanotechnology-based materials. Among nano-scale structured materials the most uncertainties are found about the thermal insulating quality of thermal insulation coatings consisted of vacuum-hollow nano-ceramic microspheres. Complete agreement had not been already found about the mechanism of their insulating effect. In order to explore and describe the thermodynamic process inside nano-ceramic coatings (NCC) 6 series of heat transfer resistance experiments were performed in 2014-2017. Several building structure configurations with 12 different orders of layers were tested with a standard heat flow meter. On basis of these results it could be concluded that in case of nano-structured materials convective heat transfer coefficient might be taken account in different way than in case of traditional macro-structured thermal insulation materials.

Keywords: nanotechnology, thermal insulation coating, nano-ceramic

1. Introduction

Nowadays, our society is facing major problems of energy and environmental aspects. Rationalizing our energy consumption and promoting the use of materials with low environmental impact are measures to be taken to slow the degradation of

our environment as well as early exhaustion of available energy resources. The building sector has over 40% of global energy consumption and 56.7% in carbon dioxide emissions, which is considerable [1] [2]. Because of these reasons regulations relating to thermal insulation performance of buildings are getting more and more rigorous in the 21st century. It has become a serious task for designers to find more effective ways for thermal insulation of buildings

The appearance of nanotechnology-based materials in architecture and civil engineering opened several possibilities in the 1990s to use them in building industry. Tensile, shear and bending strength of concrete structures can be strengthened by nanotubes or nanofibers. Nano-silica additives can increase durability and compressive strength of cement-based materials. They can be used to increase fluidity or water permeability of concrete [3] [4]. Wood-based composite materials with nanotube or nanofiber addition could have twice higher stability and mechanical strength as steel [3]. Coatings containing nanoparticle form of titanium dioxide (TiO_2) is used to build up self-cleaning surfaces [3] [4]. Nanoparticle-based coatings can also provide better adhesion, transparency, corrosion and fire protection [3] [4].

There are also several types of nanotechnology-based thermal insulation materials (e.g.; vacuum insulation panels, aerogel insulations and thermal insulation coatings consisted of vacuum-hollow nano-ceramic microspheres). Such variety of insulating products allows many possibilities to use them effectively in housing. These thermal insulation materials are generally considered to have better thermal insulation quality than traditional materials (e.g.; mineral wool products, plastic foams, etc.). Their nanostructure can hamper one or more ways of heat transport; therefore they can decrease the heat transfer coefficient of building structures [5] [6] [7] [8].

The research conducted at Széchenyi István University between 2014-2017 was intended to study the thermal insulation quality of nano-ceramic thermal insulation coatings in order to give adequate description the thermodynamic process inside its nanostructure. Chapter 2 contains a brief description about history, production and materials characteristics of nano-ceramic coatings. In the first part of Chapter 3 the paper reviews theoretical and experimental results of other authors and researchers. For better understanding, Chapter 3.1 summarizes the former experiments conducted at Széchenyi István University in 2014-2016 and then, Chapter 3.2 presents the new experiments and results. In the end, Chapter 4 contains the conclusions.

2. Thermal Insulation Coatings Consisted of Hollow Nano-Ceramic Microspheres

Among nanotechnology-based thermal insulation materials thermodynamic performance of thermal insulation coatings consisted of hollow nano-ceramic

microspheres generally generates intensive arguments in academic circles because of contradictory technical data that could be found in special literature and in producers' handouts. Complete agreement had not been already found about the mechanism of their insulating effect. Producers state that their excellent thermal insulating quality is due to their extremely low thermal conductivity [9] [10] [11]. Other researchers claim that thermal insulation coatings can highly increase heat transfer resistance of the insulated surface by reducing convective heat transfer coefficient [12]. Experiments have shown that they are able to improve the heat transfer coefficient of solid brick masonry [8].

In the early 1980s, Sridhar Komarneni and Rustum Roy [13] developed the first method of synthetizing nano-ceramics. This process called 'sol-gel' and enabled researchers to test the properties of nano-ceramics [13]. To produce nano-ceramics at a more efficient way this process was later replaced by microwave sintering [14].

The most common paint-on insulation products in Hungary contain microscopic vacuum-hollow ceramic microspheres with a diameter of 20-120 μm and with a cellular wall thickness of 50-200 nm. They were made of melted glass or ceramic on high gas-pressure and high temperature (1500 °C). After they cool down, the pressure ends, leaving a vacuum inside the microspheres. Their binding material is a mixture of synthetic rubber and other polymers. The main components are styrene (20%) and acryl latex (80%). Styrene guarantees the mechanical strength. Acryl latex makes this material resistant against weather conditions and provides flexibility. Other additives (e.g., biocides, anti-fouling and antifungal materials) make the final product durable and mold-proofed [9] [14] [15].

These coatings are typically used for exterior and interior wall insulation, but they are also suitable for pipe insulation and protection against fire and corrosion. They can be easily transmitted to hard-to-reach places [9] [15].

After mixing the ceramic microspheres with binding material, additives and water, a brush, roller or spray can be used to apply on the surface to be insulated. To assure adequate and uniform coverage, spray and roll techniques are recommended. All surfaces must be clean and free from any contamination before painting. Generally two insulating layers are required, the first of which acts as a primer layer. The drying time of a layer depends on the temperature (at 20 °C, it takes 4-5 hours). The complete solidification takes 72 hours [9] [15].

3. Heat Transfer Experiments

Special literature provides different data about thermal insulation quality of nano-ceramic coatings. Moreover, thermodynamic details are extraordinarily contradictory [16] [17]. Some sources provide that their thermal conductivity is

around 0.001-0.003 W/mK based on measurements of university laboratories in Latvia, Russia (Volgograd) and Hungary (Debrecen) [9] [10] [11]. Other sources publish much higher values (from 0.014 W/mK to 0.140 W/mK) [6] [7] [8] and more correctly talk about their effective thermal conductivity [8] [12] which contains the internal convective heat transfer coefficient (h_i) and external convective heat transfer coefficient (h_e) of the enclosed nanoscale pores inside the nanostructure. These details are often not confirmed by documented laboratory tests or refer to insufficiently introduced experiments [9] [10] [11]. Others calculate thermal conductivity of nano-ceramic coating from heat transfer coefficient (U-value) of a global building structure [8]. Each method has the same problem that it tries to determine thermal conductivity by an indirect way using conventional data and calculation and it does not take in account that physical and chemical processes inside structures in range from 1 to 100 nanometers can occur differently than in traditional macro sizes.

In order to test thermal performance of nano-ceramic coatings energy balance was investigated in periods of heating and also in the summer at external building surfaces using dynamic outdoor testing. Measurements demonstrated that coating consisting of hollow ceramic microspheres has the same thermodynamic properties as a standard facing coating [18] [19]. Spectral emissivity properties and reflective ability of nano-ceramic thermal insulation coatings were also measured with standard infrared spectroscopy and handheld reflection intensity measurement device. Measured data demonstrated that coatings have the same radiant properties as standard building coatings [20] [21]. Based on GOST 23630.2-79 (Russian standard) using an IT-λ-400 instrument thermal conductivity of nano-ceramic coatings consisted of hollow inorganic microspheres measured to be 0.10-0.18 W/mK and the effective thickness of the thin-film heat-insulation coating was determined at least 5 mm (that requires application of 4 layers of material at each layer thickness of 1-1.5 mm) [22].

3.1. Former experiments (Experiment 1, 2, 3 and 4)

Before describing the new experiments it is necessary to summarize the former results of heat transfer resistance experiments that were performed in the Laboratory of Building Materials and Building Physics at Széchenyi István University (Győr, Hungary) in 2014-2016.

After studying the special literature 4 heat transfer resistance experiments were made to explore and describe the thermodynamic process inside nano-ceramic coatings. Several building structures with different order of layers were tested with a standard heat flow meter. Results of Experiment 1, Experiment 2, Experiment 3 and Experiment 4 were published in 2015-2017 [22] [23] [24].

In Experiment 1 five types (Type 1-5) of samples were made from different kind of traditional thermal insulation materials: Expanded PolyStyrene (EPS), eXtruded PolyStyrene (XPS) and Oriented Strand Board (OSB). Sample Type 1 was uncoated and homogeneous, other samples were sprayed with nano-ceramic coating. Thermal conductivity of homogeneous samples and the effective thermal conductivity (λ_{eff}) of inhomogeneous samples (Type 2-5) were compared and results seemed to show a minor negative effect of nano-ceramic coating to thermal insulation quality. Only XPS samples showed a small positive effect with an insignificant decreasing value [23] [24].

During Experiment 2 thermal conductivity of the pure nano-ceramic coating was measured directly with a standard heat flow meter on samples with a thickness of 20 mm. The average thermal conductivity in air-dry condition was 0.0690 W/mK. However; this material is practically not used with such thickness, because they are applied as a thin membrane. Therefore it could not be clearly declared that thermal conductivity of this material has the same thermal conductivity if it is used as a very thin membrane [23].

Based on the previous two experiments it was concluded that insulating effect of nano-ceramic thermal insulation coatings is probably not caused by their extremely low thermal conductivity. As it was formerly mentioned, some sources claim that insulating effect of these materials is generated by not their extremely low thermal conductivity (this value is estimated to be 0.014 W/mK) but their high surface heat transfer resistance.

Considering it as a basic concept Experiment 3 and 4 were conducted in 2015-2016. For these experiments 12 different orders of layers were constructed from 300x300 mm samples of thermal insulation materials with different thickness. There were coated and uncoated samples; moreover, 100x100 mm air gap with a thickness of 20 and 30 mm included into the construction in Experiment 3 and 200x200 mm air gap with a thickness of 20 and 30 mm in Experiments 4. From these experiments it was expected that there should be significant differences between uncoated and coated samples and larger air gap should cause higher changes in effective thermal conductivity. Results were correspondent for expectations, and it seemed to be proven that insulating effect comes from a relatively high surface heat transfer resistance. However; insulating effect was much lower than previously expected [25].

3.2. Experiment 5 and Experiment 6

Previous experiments did not provide adequate description about thermodynamic processes inside nano-cermaic coatings. Only a relatively low thermal insulation effect was detectable. Analysing measurement data of Experiments 1-4 it was

concluded that probably the size of built-in air gaps were too small. Supposing that in a larger air gap air particles should have more possibility for bulk movements; thereby surface heat transfer resistance can prevail much better and higher differences may arise between coated and uncoated samples new experiments were conducted in 2016-2017 that were called Experiment 5 and Experiment 6.

For Experiment 5 and 6 the same order of layers were constructed from 300x300 mm samples of Thermal Insulation Materials (TIM) with 200x200 mm Air Gap (AG) with a thickness of 50 mm in Experiment 5 and with a thickness of 80 mm in Experiment 6. Because of the measuring limits (120 mm maximum sample thickness) there were only 4 Types (Types 1-4) of configurations in Experiment 6. There were configurations (Table 1), which contained Nano-Ceramic Coated (NCC) and uncoated samples as well (Type 1-6).

Table 1: Sample types for Experiment 5 and 6

Type 1	AG + TIM
Type 2	AG + NCC + TIM
Type 3	TIM + AG + TIM
Type 4	TIM + NCC + AG + TIM
Type 5	AG + TIM + AG
Type 6	AG + NCC + TIM + NCC + AG

Samples were prepared by the manufacturing company that provided only approximate data about the raw material. The composition is patented and manufacturers generally do not give completely accurate details about the product. It could be definitely stated that the examined coating was outside façade insulation. Wide limits (20-50 m/m %) were given about the ratio of the binder material, but certainly it neared the lower limit because coating was sprayed on the surface of samples and low ratio of binder material is ideal for spray technology.

According to EN 12667:2001 standard Taurus TCA 300 heat flow meter was used for measurements. Because of the inhomogeneous, multi-layer structure heat flow meter was able to determine effective thermal conductivity (λ_{eff}). Effective thermal conductivity of 3-3 pieces from each type of configurations was measured using 3 different kinds of thermal insulation materials: EPS, XPS and OSB plates. Each sample was measured 3 times. Moreover; sample Types 1-4 were measured in two ways; firstly NCC was on the warm side; secondly NCC was on the cold side. Eventually 270 different measurements were conducted in Experiment 5 and 144 in Experiment 6. Together it means a total number of 414 measurements.

Experiments 5 and 6 were to provide information about thermal insulation ability of NCC. Therefore; the main focus of experiments was the difference in effective thermal conductivity between coated and uncoated samples. Compared to Experiment 3 and 4 the only difference in configurations was the multiple increased

air gaps. Therefore; measurements of Experiments 5 and 6 were also comparable with the results of Experiment 3 and 4. Because of the increased air gap larger changes were expected in effective thermal conductivity of coated and uncoated samples.

The above assumption has been slightly proved because differences in effective thermal conductivity between coated and uncoated samples were really higher than in Experiment 3. It is well-known that the accuracy of Taurus TCA heat flow meter is up to 5% and these results might be fluctuations in measurement limits. However, in fact, in 92% there were no deviation between 3 test results of an individual sample, and in 8% the difference was only ± 0.0002 W/mK which means really 0.1-0.3% accuracy.

Table 2: Results of Experiment 3, 4, 5 and 6 with EPS samples

	Air Gap	Symbol	Unit	Type 1	Type 2	Type 3	Type 4	Type 5	Type 6
Experiment 3	**100 x 100 x 20 mm**	$\lambda_{eff,cold}$	W/mK	0.06713	0.06300	0.05470	0.05214	-	-
		$\Delta\lambda_{eff,cold}$	%	− 6.16		− 4.69		-	
		$\lambda_{eff,warm}$	W/mK	0.06691	0.06323	0.05467	0.05205	-	-
		$\Delta\lambda_{eff,warm}$	%	− 5.50		− 4.80		-	
		λ_{eff}	W/mK	0.06702	0.06312	0.05469	0.05209	0,08583	0,07840
		$\Delta\lambda_{eff}$	%	− 5.83		− 4.75		− 8.66	
	100 x 100 x 30 mm	$\lambda_{eff,cold}$	W/mK	0.08231	0.07761	0.06210	0.05902	-	-
		$\Delta\lambda_{eff,cold}$	%	− 5.71		− 4.96		-	
		$\lambda_{eff,warm}$	W/mK	0.08312	0.07830	0.06212	0.05905	-	-
		$\Delta\lambda_{eff,warm}$	%	− 5.79		− 4.94		-	
		λ_{eff}	W/mK	0.08272	0.07796	0.06211	0.05903	0.10923	0.10028
		$\Delta\lambda_{eff}$	%	− 5.75		− 4.95		− 8.19	
Experiment 4	**200 x 200 x 20 mm**	$\lambda_{eff,cold}$	W/mK	0.06475	0.06032	0.05597	0.05326	-	-
		$\Delta\lambda_{eff,cold}$	%	− 6.84		− 4.85		-	
		$\lambda_{eff,warm}$	W/mK	0.06094	0.05704	0.05594	0.05337	-	-

		$\Delta\lambda_{eff,warm}$	%	− 6.40		− 4.59		-	
		λ_{eff}	W/mK	0.06284	0.05868	0.05595	0.05331	0.07759	0.06986
		$\Delta\lambda_{eff}$	%	− 6.62		− 4.72		− 9.96	
	200 x 200 x 30 mm	$\lambda_{eff,cold}$	W/mK	0.08046	0.07523	0.06612	0.06273	-	-
		$\Delta\lambda_{eff,cold}$	%	− 6.50		− 5.14		-	
		$\lambda_{eff,warm}$	W/mK	0.07791	0.07361	0.06613	0.06289	-	-
		$\Delta\lambda_{eff,warm}$	%	− 5.52		− 4.90		-	
		λ_{eff}	W/mK	0.07919	0.07442	0.06613	0.06281	0.10830	0.09526
		$\Delta\lambda_{eff}$	%	− 6.01		− 5.02		− 12.04	
Experiment 5 & 6	200 x 200 x 50 mm	$\lambda_{eff,cold}$	W/mK	0.010740	0.09775	0.08369	0.07870	-	-
		$\Delta\lambda_{eff,cold}$	%	− 8.99		− 5.97		-	
		$\lambda_{eff,warm}$	W/mK	0.10633	0.09823	0.08381	0.07962	-	-
		$\Delta\lambda_{eff,warm}$	%	− 7.88		− 5.00		-	
		λ_{eff}	W/mK	0.10702	0.09799	0.08375	0.07916	0.15810	0.13780
		$\Delta\lambda_{eff}$	%	− 8.43		− 5.48		− 12.84	
	200 x 200 x 80 mm	$\lambda_{eff,cold}$	W/mK	0,14923	0,12730	0,11283	0,10353	-	-
		$\Delta\lambda_{eff,cold}$	%	− 14.70		− 8.24		-	
		$\lambda_{eff,warm}$	W/mK	0,16383	0,14617	0,11290	0,10557	-	-
		$\Delta\lambda_{eff,warm}$	%	− 10.78		− 6.50		-	
		λ_{eff}	W/mK	0,15653	0,13673	0,11287	0,10455	-	-
		$\Delta\lambda_{eff}$	%	− 12,74		− 7,37		-	

Effective thermal conductivity changes caused by nano-cermaic coating were the most apparent in EPS samples (Table 2). In Experiment 5 the most significant difference in effective thermal conductivity (12.84%) was found between configuration Type 5 and configuration Type 6 due to the two-sided nano-ceramic coating. As it was formerly expected, higher changes were registered than in Experiment 3 and 4. In case of Types 1-2 change level was also higher (8.99% on cold side and 7.88% on warm side in Experiment 5 and 14.70% on cold side and 10.78% on warm side in Experiment 6) than Experiment 3 and 4. Effective thermal conductivity changes were also the lowest in case of Types 3-4 (5.97% on cold side

and 5.00% on warm side in Experiment 5 and 8.24% on cold side and 6.50% on warm side in Experiment 6) but despite of Experiment 3 and 4 these values were more significant. This phenomenon can be explained that if an air gap is closed inside two layers of thermal insulation air particles are less able to move and the effect of surface heat transfer resistance becomes smaller. It can be also concluded that the application of NCC in this way could be the least efficient. In Experiment 6 remarkably higher changes were registered that was probably caused by the much thicker (80 mm) air gap. Contrary to the past experiments there were evincible differences between measurement results depending on the location of the coating (warm or cold side). In former experiments with smaller air gaps (20 and 30 mm) effective thermal conductivity was measured the same regardless whether the coating was on the cold or warm side. New results showed that nano-ceramic coating has stronger effect on the cold side.

In case of XPS samples smaller changes can be observed (Table 3) similarly to Experiment 3 and 4. This could be explained by the results of Experiment 1 where nano-ceramic coating itself had resulted reduction of thermal conductivity. This is why surface heat transfer resistance seems to have minor effect on thermal insulation quality. Change of thermal conductivity was the most significant in configuration Types 1-2 (6.17% on the cold side and 4.00% on the warm side in Experiment 5 and 8.91% on the cold side and 8.90% on the warm side in Experiment 6). Configuration Types 5-6 showed also higher changes than in Experiment 3 and 4 but the increase was not as significant as in case of EPS samples (4.53%). Just like EPS samples, a little bit lower changes were measured in case of Types 3-4 (3.73% and 2.38% in Experiment 5, and 5.02% and 3.49% in Experiment 6). There were also similar detectable differences to EPS samples between measurement results depending on the location of the coating (warm or cold side).

Table 3: Results of Experiment 3, 4, 5 and 6 with XPS samples

	Air Gap	Symbol	Unit	Type 1	Type 2	Type 3	Type 4	Type 5	Type 6
Experiment 3	100 x 100 x 20 mm	$\lambda_{eff,cold}$	W/mK	0.05148	0.04964	0.04534	0.04369	-	-
		$\Delta\lambda_{eff,cold}$	%	− 3.57		− 3.64		-	
		$\lambda_{eff,warm}$	W/mK	0.05139	0.04968	0.04578	0.04425	-	-
		$\Delta\lambda_{eff,warm}$	%	− 3.33		− 3.34		-	
		λ_{eff}	W/mK	0.05154	0.04966	0.04556	0.04397	0.06456	0.06276
		$\Delta\lambda_{eff}$	%	− 3.45		− 3.49		− 2.79	
	1 0	$\lambda_{eff,cold}$	W/mK	0.06233	0.06021	0.05053	0.04874	-	-

		$\Delta\lambda_{eff,cold}$	%	− 3.40		− 3.53		-	
		$\lambda_{eff,warm}$	W/mK	0.06208	0.06034	0.05131	0.04968	-	-
		$\Delta\lambda_{eff,warm}$	%	− 2.80		− 3.16		-	
		λ_{eff}	W/mK	0.06220	0.06027	0.05092	0.04921	0.08259	0.08033
		$\Delta\lambda_{eff}$	%	− 3.10		− 3.35		− 2.74	
Experiment 4	200 x 200 x 20 mm	$\lambda_{eff,cold}$	W/mK	0.04856	0.04592	0.04594	0.04430	-	-
		$\Delta\lambda_{eff,cold}$	%	− 5.44		− 3.56		-	
		$\lambda_{eff,warm}$	W/mK	0.04666	0.04445	0.04725	0.04585	-	-
		$\Delta\lambda_{eff,warm}$	%	− 4.95		− 2.97		-	
		λ_{eff}	W/mK	0.04761	0.04513	0.04660	0.04508	0.05641	0.05431
		$\Delta\lambda_{eff}$	%	− 5.19		− 3.27		− 3.71	
	200 x 200 x 30 mm	$\lambda_{eff,cold}$	W/mK	0.05972	0.05670	0.05262	0.05044	-	-
		$\Delta\lambda_{eff,cold}$	%	− 5.06		− 4.14		-	
		$\lambda_{eff,warm}$	W/mK	0.05850	0.05568	0.05521	0.05363	-	-
		$\Delta\lambda_{eff,warm}$	%	− 4.82		− 2.87		-	
		λ_{eff}	W/mK	0.05911	0.05619	0.05391	0.05203	0.07689	0.07310
		$\Delta\lambda_{eff}$	%	− 4.94		− 3.51		− 4.92	
Experiment 5 & 6	200 x 200 x 50 mm	$\lambda_{eff,cold}$	W/mK	0.07623	0.07153	0.06323	0.06110	-	-
		$\Delta\lambda_{eff,cold}$	%	− 6.17		− 3.73		-	
		$\lambda_{eff,warm}$	W/mK	0.07767	0.07456	0.07157	0.06987	-	-
		$\Delta\lambda_{eff,warm}$	%	− 4.00		− 2.38		-	
		λ_{eff}	W/mK	0.07695	0.07305	0.06740	0.06582	0.10367	0.09897
		$\Delta\lambda_{eff}$	%	− 5.08		− 2.87		− 4.53	
	200 x 200 x 80 mm	$\lambda_{eff,cold}$	W/mK	0.09192	0.08373	0.06533	0.06205	-	-
		$\Delta\lambda_{eff,cold}$	%	− 8.91		− 5.02		-	
		$\lambda_{eff,warm}$	W/mK	0.11383	0.10370	0.07571	0.07307	-	-

	$\Delta\lambda_{eff,warm}$	%	− 8.90		− 3.49		-	
	λ_{eff}	W/mK	0.10288	0.09372	0.07052	0.06756	-	-
	$\Delta\lambda_{eff}$	%	− 8.91		− 4.26		− 3.10	

In case of OSB boards insulating effect of nano-ceramic coating was undetectable (Table 4). Except sample Types 5-6, all measurements showed that coating has a negative effect on thermal insulation quality. It can be observed that this negative effect decreases by increasing the thickness of the air gap. Analyzing the results of Types 3-4 it can be observed that in case of 20 mm air gap NCC increased effective thermal conductivity with 2.82% in Experiment 3, and 3.08% in Experiment 4. With 30 mm air gap this value was 2.83% in Experiment 3 (it is nearly the same) but 2.68% in Experiment 4. In Experiment 5 this value decreased to 1.88% and in Experiment 6 to 1.05%. Measurement results of Types 5-6 show that with two-sided 20 mm air gap NCC increased effective thermal conductivity with 2.29% in Experiment 3 and 2.16% in Experiment 4. With 30 mm air gap this value decreased to 1.21% in Experiment 3 and to -0.02% (i.e.; nearly zero) in Experiment 4. Using 50 mm air gap a very small decreasing of effective thermal conductivity was detected (-1.04%).

On basis of these results it could be concluded that NCC requires a much larger air gap in order to have beneficent thermal insulation effect on OSB plates. It can be also admitted that thermal insulation effect of NCC could be very different on different types of surfaces.

Table 4: Results of Experiment 3, 4, 5 and 6 with OSB samples

	Air Gap	Symbol	Unit	Type 1	Type 2	Type 3	Type 4	Type 5	Type 6
Experiment 3	100 x 100 x 20 mm	$\lambda_{eff,cold}$	W/mK	0.10517	0.10910	0.06674	0.06845	-	-
		$\Delta\lambda_{eff,cold}$	%	+ 3.74		+ 2.57		-	
		$\lambda_{eff,warm}$	W/mK	0.10743	0.11033	0.06946	0.07160	-	-
		$\Delta\lambda_{eff,warm}$	%	+ 2.70		+ 3.08		-	
		λ_{eff}	W/mK	0.10630	0.10972	0.06810	0.07003	0.11800	0.012070
		$\Delta\lambda_{eff}$	%	+ 3.22		+ 2.82		+ 2.29	
	100 x 100 x 30 mm	$\lambda_{eff,cold}$	W/mK	0.12597	0.12827	0.07347	0.07571	-	-
		$\Delta\lambda_{eff,cold}$	%	+ 1.83		+ 3.04		-	
		$\lambda_{eff,warm}$	W/mK	0.012723	0.13093	0.07756	0.07960	-	-

		$\Delta\lambda_{eff,warm}$	%	+ 2.91		+ 2.63		-	
		λ_{eff}	W/mK	0.12660	0.12960	0.07552	0.07765	0.15097	0.15280
		$\Delta\lambda_{eff}$	%	+ 2.37		+ 2.83		+ 1.21	
Experiment 4	200 x 200 x 20 mm	$\lambda_{eff,cold}$	W/mK	0.09991	0.10463	0.07041	0.07214	-	-
		$\Delta\lambda_{eff,cold}$	%	+ 4.72		+ 2.45		-	
		$\lambda_{eff,warm}$	W/mK	0.10997	0.11330	0.07287	0.07557	-	-
		$\Delta\lambda_{eff,warm}$	%	+ 3.03		+ 3.71		-	
		λ_{eff}	W/mK	0.10494	0.10897	0.07164	0.07385	0.10643	0.10873
		$\Delta\lambda_{eff}$	%	+ 3.88		+ 3.08		+ 2.16	
	200 x 200 x 30 mm	$\lambda_{eff,cold}$	W/mK	0.12090	0.012450	0.08209	0.08411	-	-
		$\Delta\lambda_{eff,cold}$	%	+ 2.98		+ 2.46		-	
		$\lambda_{eff,warm}$	W/mK	0.012847	0.13427	0.08549	0.08798	-	-
		$\Delta\lambda_{eff,warm}$	%	+ 4.51		+ 2.91		-	
		λ_{eff}	W/mK	0.12468	0.12938	0.08379	0.08605	0.14140	0.14137
		$\Delta\lambda_{eff}$	%	+ 3.75		+ 2.68		− 0.02	
Experiment 5 & 6	200 x 200 x 50 mm	$\lambda_{eff,cold}$	W/mK	0.016100	0.016667	0.10400	0.10570	-	-
		$\Delta\lambda_{eff,cold}$	%	+ 3.52		+ 1.63		-	
		$\lambda_{eff,warm}$	W/mK	0.17167	0.18000	0.11000	0.11233	-	-
		$\Delta\lambda_{eff,warm}$	%	+ 4.85		+ 2.12		-	
		λ_{eff}	W/mK	0.16633	0.17333	0.10700	0.10902	0.19267	0.19067
		$\Delta\lambda_{eff}$	%	+ 4.19		+ 1.88		− 1.04	
	200 x 200 x 80 mm	$\lambda_{eff,cold}$	W/mK	0.23667	0.24153	0.14827	0.14967	-	-
		$\Delta\lambda_{eff,cold}$	%	+ 2.06		+ 0.94		-	
		$\lambda_{eff,warm}$	W/mK	0.22987	0.23550	0.15267	0.15443	-	-
		$\Delta\lambda_{eff,warm}$	%	+ 2.45		+ 1.16		-	
		λ_{eff}	W/mK	0.23327	0.23851	0.15047	0.15205	-	-
		$\Delta\lambda_{eff}$	%	+ 2.25		+ 1.05		-	

4. Discussion

Nano-ceramic coatings cause plenty of scientific discussion between architects because there is no accepted consensus about their thermal insulating quality. In addition, a wide variety of manufacturers and distributors provide contradictory material properties in their product brochures. Manufactureres generally do not explain how material properties are measured and they often do not refer scientifically accepted special literature. They also do not give satisfying information about material composition; therefore it is often difficult to decide exactly which type of material is involved [9] [10] [11].

Numerous theoretical and experimental researches have been conducted in the past few years and results have raised several questions. Researchers did not reveal any difference between thermal insulation quality of conventional paints and nano-ceramic coatings with energy balance calculations, spectral emissivity and reflective ability measurements of nano-ceramic thermal insulation coatings [18] [19] [20] [21]. Thermal conductivity was indirectly calculated from measurements of heat transfer coefficient but obtained values were quite different (0.00177 W/mK and 0.10-0.18 W/mK) [9] [11] [22].

Some theoretical papers explain thermal insulating ability of nano-ceramic coatings not with its low thermal conductivity, but with its high surface heat transfer resistance. These papers claim that as a result of the nanostructure, heat transfer process on the inside and outside surface of nano-ceramic coating becomes different from traditional macrostructured materials and internal and external surface heat transfer coefficient recommended by the standards (h_i = 8 W/m^{2}K and h_e = 24W/m^{2}K) have to be changed [6] [7] [12] [17].

Former laboratory tests (Experiment 1 and Experiment 2) conducted in 2014-2015 in the Laboratory of Building Materials and Building Physics at Széchenyi István University showed that nano-ceramic thermal insulation coatings probably do not have an extremely low thermal conductivity that was described by the available documents of producers and distributors. Their thermal conductivity is likely to be higher than that of traditional thermal insulation materials like mineral wool products or plastic foams (e.g. EPS, XPS and polyurethane foam) [23].

Former thermodynamic experiments (Experiment 3 and Experiment 4) in 2014-2016 were partially seemed to prove the hypothesis of some special literature sources that insulating effect of nano-ceramic coatings comes from a relatively high surface heat transfer resistance because in some sample configurations, where an air gap was inserted, effective thermal conductivity of coated samples was lower than the uncoated samples. These results based the following series of measurements that were conducted in 2016-2017[24] [25].

5. Conclusions

New series of thermodynamic experiments (Experiment 5 and Experiment 6) in the Laboratory of Building Physics and Building Materials at Széchenyi István University (Győr, Hungary) were conducted to prove or disprove the hypothesis of high surface heat transfer resistance. However; it can be seen that the difference of effective thermal conductivity between coated and uncoated samples were getting more significant when the size of the air gap is increasing.

It can be observed that in the case of a surface from low-density material (e.g.; EPS), 50-80 mm air gap might have a significant effect (8.99-14.70%). When NCC is applied on a surface with medium density (e.g.; XPS) thicker air gap is needed. Applying it on a high-density surface (e.g.; OSB plate) NCC has positive effect on effective thermal conductivity only with two-sided 80 mm air gap material. Presumably with an infinite air gap (e.g.; on the outside surface of masonry structure) insulating effect of NCC would be much more intensive.

Experiments 5 and 6 confirmed the former assumption based by Experiment 4 that higher heat transfer resistance of coated samples caused by the lower surface convective heat transfer coefficient. It can be declared that in case of nano-structured materials convective heat transfer coefficient might be taken account in different way than in case of traditional macro-structured thermal insulation materials.

Test results also showed that thermal insulating ability of this material prevails otherwise on different kind of surfaces. Insulation effect depends not only on the thickness of the air gap but also on the material of the insulated surface. Presumably the same material quality, composition and application technology may not be suitable for insulating different kind of surfaces. Every time we need to find correct solution and definitely the same material is not suitable for all surfaces.

Further studies are needed to have quantified data about the insulation effect of NCC. It would be important to make in-situ heat transfer experiments (Experiment 7) with NCC for better understanding the thermal insulation behavior of it. In order to achieve this goal heat transfer coefficient of several sample buildings should be measured without any thermal insulation. These basic data should be compared with the heat transfer coefficient of structures with NCC insulation. Based on previous (Experiments 1-6) and future tests (Experiment 7) a specific value of external and internal convective heat transfer coefficient (he and hi) should be calculated. Experiments and analysis are still running. Results will be reported in a subsequent study.

Acknowledgement

References

[1] R. Belakroun, A. Gherfia,Y. Kerboua, M. Kadja, T. H. Mai, C. Maalouf, B. Mboumba-Mamboudou,M. T'kint, Experimental investigation of mechanical and thermal properties of a new biosourced insulation material, International Scientific Journal of Environmental Science 4 (2015) pp. 78-81.

[2] A. Shea, M. Lawrence, P. Walker, Hygrothrermal performance of an experimental hemp-lime building, Construction and Building Materials 36 (2012) pp. 270-275.
doi: 10.1016/j.conbuildmat.2012.04.123

[3] F. Pacheco-Torgal, S. Jalali, Nanotechnology: Advantages and drawbacks in the field of construction and building materials, Construction and Building Materials 25 (2) (2011) pp. 582−590.
doi: 10.1016/j.conbuildmat.2010.07.009

[4] M. Abdelrahman, Towards sustainable architecture with nanotechnology, Al-Azhar Engineering 11th International Conference, Cairo, Egypt, 21-23 December 2010, paper 154.

[5] P. B. Jelle, A. Gustavsen, S. Grynning, E. Wegger, E. Sveipe, R. Baetens, Nanotechnology and Possibiles for the Thermal Building Insulation Materials of Tomorrow, In: Haase M., Hestnes A. G. (Eds), Renewable Energy Research Conference 2010 – Zero Emission Buildings, 7-8 June 2010, Trondheim (Norway), Norwegian University of Science and Technology & Tapir Academic Press, ISBN 978-82-519-2623-2, 2010, pp. 121-132.

[6] J. Orbán, Use of nanotechnology in building industry, Part I. (in Hungarian), Magyar Építéstechnika 50 (1) (2012) pp. 40−43.

[7] J. Orbán, Use of nanotechnology in building industry, Part II. (in Hungarian), Magyar Építéstechnika 50 (2-3)(2012) pp. 54−57.

[8]   Á. Lakatos, Examination of nanotechnology-based thermal insulation materials on solid brick masonry (in Hungarian), Energiagazdálkodás 57 (3-4)(2016) pp. 21-25.

[9]   Thermogát Ltd.: Thermal insulating process of TSM Ceramic coating; Thermogát Ltd., Budapest (Hungary) [cited 2017-05-14] URL http://tsmceramic.com/?modul=oldal&tartalom=1196370

[10] Thermo-Shield Inc.: Exterior wall coats, SPM Thermo-Shield Inc., Naples (Florida, United States) [cited 2017-05-05] URL http://www.thermoshield.com/index.html/thermoshieldexteriorwall.html

[11] MANTI Ceramic Ltd.: Thin-layer thermal protection (in Hungarian), MANTI Ceramic Ltd., Budaörs (Hungary), 2016, p. 20 [cited 2017-05-14] URL https://www.manti.hu/press

[12] J. Orbán, Reducing energy consumption of buildings with the help of thin heat protection coatings, Part II (in Hungarian), Magyar Építéstechnika 9 (2015) pp. 40−42.

[13] D. Hoffman, R. Roy, S. Komarneni, Diphasic ceramic composites via a sol-gel method, Materials Letters 2 (3) (1984) pp. 245−247. URL https://doi.org/10.1016/0167-577X(84)90035-1

[14] L. I. C. Sandberg, T. Gao, B. P. Jelle, A. Gustavsen, Synthesis of hollow silica nanospheres by sacrificial polystyrene templates for thermal insulation applications, Advances in Material Science and Engineering (2013) p. 6. Article ID 483651 URL http://dx.doi.org/10.1155/2013/483651

[15] W. Lan. F. Kexing, Y. Liang, W. Botao, The application of ceramic coatings in petroleum chemical and building industries, International Conference on Material and Environmental Engineering, 21-24 March 2014, Jiujiang (Jiangxi, China), Atlantis Press, pp. 146−149 doi: 10.2991/icmaee-14.2014.39

[16] G. Paul, M. Chopkar, I. Manna, P. K. Das, Techniques for measuring the thermal conductivity of nanofluids, A Review, Renewable and Sustainable Energy Reviews 14 (7) (2010) pp. 1913−1924. doi: https://doi.org/10.1016/j.rser.2010.03.017

[17] P. Koniorczyk, J. Zmywaczyk, M. Kowalski, Experimental studies of thermal conductivity of the composite coating consisted of hollow ceramic microspheres, In: Walczok W. (Ed.): 1st Scientific International Coating Congress, 4-5 November 2004, Berlin (Germany), p. 15.

[18] M. Čekon, Thermodynamic Properties of Reflective Coatings, Advanced Materials Research 649 (2013) pp. 179-182
doi: 10.4028/www.scientific.net/AMR.649.179

[19] M. Čekon, M. Kalousek, J. Hraška, R. Ingeli, Spectral optical properties and thermodynamic performance of reflective coatings in a Mild Climate Zone, Energy and Buildings 77 (2014) pp. 343-354.
doi: https://doi.org/10.1016/j.enbuild.2014.04.005

[20] M. Čekon, Spectral emissivity properties of reflective coatings, Slovak Journal of Civil Engineering 20 (2) (2012) pp. 1-7.
doi: https://doi.org/10.2478/v10189-012-0007-6

[21] L. Ádám, B. Nagy, R. Nemes, Laboratory experiments and development possibilities of reflective coatings (in Hungarian), Megtérülő Épületenergetika 3 (7) pp. 35-39.

[22] V. Y. Chukhlanov, T. A. Trifonova, O. G. Selivanov, M. E. Ilina, N. V. Chukhlanova, Thin-Film Coatings Based on Hollow Inorganic Microsheres and Polyacrilic Binder, International Journal of Applied Engineering Research 12 (7) (2017) pp. 1194-1199.

[23] D. Bozsaky, Laboratory test with liquid nano-ceramic thermal insulation coating, Procedia Engineering 123 (2015) pp. 68−75.
doi: https://doi.org/10.1016/j.proeng.2015.10.059

[24] D. Bozsaky, Thermodynamic tests with nano-ceramic thermal insulation coatings, Pollack Periodica 12 (1) (2017) pp. 135-145.
doi: https://doi.org/10.1556/606.2017.12.1.11

[25] D. Bozsaky, Heat transfer resistance experiments of thermal insulation coatings consisted of hollow nano-ceramic microspheres, In: NANOTEK 2017 Bioleagues Worldwide Conference, 11-13 March 2017, Hamburg (Germany), ISBN 978-81-932966-1-5, 2017, pp. 9-18.

Determination of Safety Factors for Mango Fruit Paperboard Transport Crates under Refrigerated Conditions

B. Sadlowsky[1], V. Köstner[1,2], M. Mazur[1], S. Thun[3], P. Böröcz[4]

[1]BFSV Verpackungsinstitute Hamburg
Ulmenliet 20, 21033 Hamburg, Germany

[2]University of Hamburg, Department of Wood Science
Mittelweg 177, 20148 Hamburg, Germany

[3]Hamburg University of Applied Sciences, Department of Nutrition and Home Economics
Ulmenliet 20, 21033 Hamburg, Germany

[4]Széchenyi István University, Department of Logistics and Forwarding
Egyetem sq. 1, 9026 Győr, Hungary
Phone: +36 96 503 400
e-mail: boroczp@sze.hu

Abstract: The use of corrugated board packaging is very popular in most industry sectors, but the food industry is one of the main consumers. Special requirements are placed on corrugated board in the food industry since the level of humidity necessary may be as high as 85-90% RH and this can greatly influence on the performance of the packaging. This influencing circumstance is taken into account in this paper when estimating a safety factor aimed at reducing risk. Knowing the safety factor can save transport and material costs, and can also prevent serious damage during the distribution of goods. The aim of this study is to determine the influence of humidity, pre-compression and load carriers on the stability of corrugated board mango fruit crates and thus to determine the safety factor. The results show that it is possible to calculate the safety factor by measuring realistic static stresses. Further

researches into determining the dynamic stresses are required so as completing the calculation of the safety factor.

Keywords: safety factor, corrugated board, mango fruit crate

1. Introduction

Corrugated board packaging is the most popular packaging material in the distribution of industrial food products [1]. In addition to low weight and high stability, the corrugated board is environmentally friendly and very versatile in its function and use [2]. It will continue to be used in a number of industries in the future [1].

Packaging, which is made of corrugated board protects the food during transport and also has a product presentation function in the food industry [3]. A damaged package can decrease the sales value even if the product itself is free from defects [4]. Exposure to transport, handling and storing (THS) loads expose the packaging to stresses on a daily basis [5]. These stresses lead to deformation [6], compression and cracking of the packaging material, or to damages of product. To choose an appropriate packaging material requires knowledge of the conditions under which the food is transported. There is a particularly critical correlation between the quality of the corrugated board and the humidity of the environment or high-moisture foods [7][8]. Corrugated board loses its stability and structure, including detachment of the individual layers of paper, if the humidity level of the environment is too high or if the material comes into direct contact with water.

The investigation of single package under normal climatic conditions (23 °C and 50% RH) and any assessments derived from them with regard to the stability of similar corrugated boards under other climatic conditions may be inadequate. It is necessary to consider using a safety factor to reduce the risk of damage [8].

In the literature, there is a paper of Chonhenchob, in 2004, which dealt with the testing of various distribution packaging of mangos such as plastic crate, bamboo basket and corrugated box. The aim of that study was to compare the protection method of different types and to present an economic comparison of various packaging system [9]. Another paper of Chonhenchob evaluated the differences between corrugated boxes and plastic container. The results of that study indicated that proper shipping container and cushioning methods how to reduce bruising in mangoes [10]. Other papers analysed the effect of physical environment in distribution to mangoes such as transport vibration [11]. But the authors of this paper could not find any research on the compression strength of paperboard crates for mangoes with applicable safety factor with the aspect of refrigerated conditions.

This study is concerned with determining safety factor for corrugated board mango fruit crates. Static stress conditions will be imitated by short-term BCT measurement of single crates and load units with high humidity under refrigerated conditions. Dynamic stresses are not considered in this investigation. The measurements are based on the climatic requirements of mango fruits (11°C and 87% RH).

2. Methods

2.1. Materials

The samples were corrugated board mango fruit crates (FEFCO 0422-V, DIN 55468-1:2015 2.50 BC flute) equipped with stacking noses. These were cut off the upper crates of a unit load for BCT measurements. The internal dimensions of the fruit crates were: 452 x 383 x 215 [mm] (length x width x height).

2.2. Loading units

The same euro-pallets (800 x 1200 mm) were used for all measurements, can be seen in Figure 1. Considering the outer dimensions of the crates (490 x 390 x 220 mm) and potentially bulges (10 mm), 4 crates were packed at each layer. There was a remaining area of 200 x 800 mm, which meets an 83% rate of use. The crates were not modular. The loading unit was limited to a height of 1500 mm, this way 6 crates were stacked. In total, there were 24 crates packed centrally on each pallet.

2.3. Packaged goods

The crates were filled with 12.5 kg cider apples to simulate a realistic punctual weight strain by mango fruits.

2.4. Experiment setup

The mechanical properties of the corrugated board used for the fruit crates were analysed by measuring BCT, ECT, bursting strength and puncture resistance. Furthermore, the paper quality and water resistance were tested to check wet-strength gluing.

The determination of short-term BCT values was conducted as described in DIN 55440-1:1991-11. The BCT values for investigating the mechanical properties of corrugated fibreboard were determined using single crates. This measurement was performed in 23/50 climate pairs only. Unit loads of fruit crates were measured in 23/50 and 11/87 climate pairs. The upper crates of unit loads with a pallet top and bottom were secured with a tension belt.

The short-term BCT values for three different unit loads of fruit crates were determined in a 23/50 (Method A) and 11/87 (Method B) climate conditions. Taking the outer dimensions of the crates (490 x 390 x 220 mm) and any potential bulges (10 mm) into consideration, 24 crates were packed centrally on each pallet (Euro pallets 800x1200 mm). The crates were filled with 12.5 kg cider apples to simulate a realistic concentrated point load exerted by mango fruits. The 11/87 climate pairs were within the range of an optimum climate for mango fruits [12]. Both climates were compared, allowing for the influence of weight and load carriers on the crates. The unit loads were stressed using packed goods. The method was repeated without packed goods in a 23/50 climate pairs (Method C). The list and Figure 1 below illustrates the overall conditions described above.

(1) Load unit without carrier (Method A, B and C)

(2) Load unit with carrier on the bottom (Method A, B and C)

(3) Load unit with carrier on the bottom and top (Method A, B and C)

Method A: 23/50, Method B: 11/87, Method C: 23/50 without packed goods

(1)   (2)   (3)

Figure 1. Test setup for fruit crates

The results of the mechanical properties of the fruit crates were averaged and are shown in Table 1. The TAPPI test was performed on the packaging material since the single layers of paper did not detach after 24 hours of water influence.

Table 1. Averaged values for the mechanical properties of the fruit crates (FEFCO 0422-V)

	Bursting strength (kPa)	*Puncturing Energy (J)*	*ECT (kN/m)*	*BCT (N)*
Avg.	1 433	9.2	11.0	7 389
S	58.4	0.3	0.3	629.7

v	4.5	2.6	2.4	8.5

Table 2 and 3 contains the results of BCT measurements for each unit load type and climate. All the unit loads that were air-conditioned in 11/87 climates and stressed with packed goods (1-3b) showed the lowest BCT values, while the unit loads without packed goods in 23/50 climates (1-3c) displayed the highest. The other unit loads in the 23/50 climates, which were stressed with packed goods (1-3a) show lower results than 'c' but higher than 'b'. At any rate, the results for 'a' and 'c' are similar considering the standard deviation but 'c' has higher displacement values than 'a'. The standard deviation for (1c) is very high compared to all the other standard deviations.

Table 2. BCT values of unit loads without pallet (1); with pallet on the bottom (2); with pallet on the bottom and top (3)

	F_{max} (N)	Displacement (mm)	Avg. (N)	S (N)	V (%)
Method A (23/50 – with packed goods)					
(1)	19 151	67	18 997	810.7	4
	20 527	70			
	19 523	72			
(2)	18 674	70	19 734	711.8	3
	19 919	67			
	18 397	66			
(3)	20 299	71	20 249	417.8	2
	19 808	68			
	20 639	70			
Method B (11/87 – with packed goods)					
	F_{max} (N)	Displacement (mm)	Avg. (N)	S (N)	V (%)
(1)	10 705	69	10 634	367.1	4
	10 237	65			
	10 961	71			
(2)	11 642	69	11 522	192.5	2
	11 624	66			
	11 300	67			
(3)	11 074	81	11 038	180.7	2
	11 198	75			
	10 842	75			

Table 3. BCT values of unit loads without pallet (1); with pallet on the bottom (2); with pallet on the bottom and top (3)

	F_{max} (N)	Displacement (mm)	Avg. (N)	S (N)	V (%)
Method C (23/50 – without packed goods)					
(1)	19 317	95	19 701	1834.9	9
	18 089	90			
	21 698	90			
(2)	20 841	88	20 645	291.3	1
	20 783	88			
	20 310	90			
(3)	21 019	104	21 035	206.9	1
	20 836	90			
	21 249	88			

3. Discussion

3.1. Effect of climate and load carrier

Figure 3 shows the results of the BCT measurements for fruit crate unit loads in 23/50 (with and without packed goods) and 11/87 (with packed goods) climate overall.

There are small differences (3.9%) between the results of unit loads that were measured in 23/50 climate pairs with and without packed goods. Crates that were stressed with packed goods (a) displayed a lower compression path (69 mm) compared to those without packed goods (c) (91 mm). This is caused by the pre-compression of the crates due to the packed goods.

The climate had a significant influence on the crush resistance of the crates that were air-conditioned in 11/87 climate pairs (b). The values of these crates were up to 45.5% lower than their counterparts (a) as a result of high humidity and pre-compression. It was estimated that the load carriers would exert additional stress on the units due to the alternately missing linear boards of the Euro pallet at the bottom (2) or due to additional weight on the top of the load unit (3). At any rate, there was a very small difference between experimental setup (2) and (3) in 23/50 climate pairs.
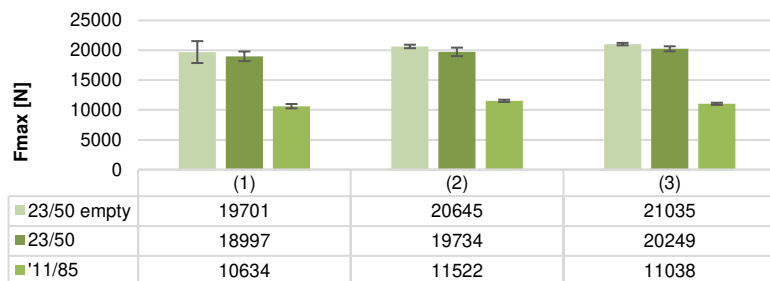
	(1)	(2)	(3)
23/50 empty	19701	20645	21035
23/50	18997	19734	20249
'11/85	10634	11522	11038

Figure 3. Summary for examined BCT force [N] of fruit crates units (Type FEFCO 0422-V)

The upper pallet was placed precisely over the corners of the crates, which were the strongest part of the packaging. This protected the weaker parts of the crates against compression hazards. Without a pallet the force was distributed simultaneously over the corners as well as the sidewalls, which led to lower results among the stacking systems without a pallet (1).

Unexpectedly, the highest BCT values for unit loads that were air-conditioned in 11/87 climate pairs (Method B) were measured for a unit load with a carrier at the bottom (2). An additional carrier at the top stressed the unit (3). The humidity softened the material so that the compression force affected it more than crates that were air-conditioned in 23/50 climate pairs.

3.2. Safety factor

A safety factor of 3-5 was estimated in advance for the mango fruit crates in a standard climate. The safety factor based on this study takes account of static stresses on unit loads. Dynamic stresses were not considered. A value of 7389 N was determined by measuring the BCT of single fruit crates. Four fruit crates were packed on each layer. Thus, ultimately, a BCT of 7389 N x 4 layer = 29556 N should have been measured for a unit load. The highest BCT value was 21035 N, which means a loss of 29% due to stacking the crates in a unit load. This shows that this calculation and estimating the safety factor based on experience is inadequate. Stacking of the individual crates also influences the BCT values and cannot be estimated.

To calculate a safety factor that takes account of realistic stresses on the packages, it is necessary to describe the THS stresses in as much detail as possible. Thus the safety factor must be calculated individually for each packaging and transport

situation. The safety factor is usually estimated using a formula as provided by the VDA (German Association of the Automotive Industry) [13]:

$$S = \frac{loadability\ (BCT,23/50)}{acceptable\ extra\ load} \qquad (1)$$

Based on the VDA formula, a more detailed calculation is possible. A calculation for the safety factor can be formulated by considering the dynamic and static stresses:

$$S \geq S_{static} + S_{dynamic} \qquad (2)$$

In this study, the static stress of corrugated board fruit crates was realistically imitated by measuring the BCT values of unit loads using apples as the packed goods in the optimum climate for mangoes. Taking these circumstances into account, the static safety factor can be defined as:

$$S_{stat} = \frac{loadability\ (BCT,23/50) \cdot packaging\ on\ each\ layer}{loadability\ (BCT_{LU}, individual\ climate)} \qquad (3)$$

Unit load 3b is the most realistic stacking system in this study since it simulates the climate (11/87), weight and the stacking of a further unit load on top of it. The following calculation is an example of applying the formula defined above (Eq. 3) in relation to unit load 3b. The result of the calculation is as follows:

$$S_{stat} = \frac{7389N \cdot 4}{11038N} = 2.7 \qquad (4)$$

Table 4. Calculated static safety factors for unit loads: (1) without pallet, (2) with pallet on the bottom, (3) with pallet on the bottom and top.

	Method A 23/50	*Method B* 11/87	*Method C* 23/50 (*empty*)
(1)	1.6	2.8	1.5
(2)	1.5	2.6	1.4
(3)	1.5	2.7	1.4

A higher risk is expressed by a higher static safety factor as shown in the results above. The high humidity affects the packaging and therefore increases the values of the static safety factors for crates that were air-conditioned in 11/87 climate pairs. It is also necessary to determine the dynamic safety factor to complete the calculation and to properly define the safety factor.

4. Conclusion

The results of the tested corrugated board mango fruit crates conclude the following general statements. Estimating the safety factor by measuring the BCT of single crates can be easily inadequate. It is necessary to determine the BCT under realistic conditions as shown in this study. The relative humidity, weight and stacking system have a significant influence on the performance of a packaging material. It is necessary to measure these effects individually for each packaging and stacking system. The static safety factor can be calculated based on static stress values. Further research is required to determine the dynamic stresses and thus to complete the presented calculation.

Acknowledgement

References

[1] Verband der Wellpappen-Industrie e.V., Die wichtigsten Zahlen für die Wellpappenindustrie (2015) [cited 2018-01-16]
URL http://wellpappen-industrie.de/data/04_Verband/05_Publikationen/03_ZahlenFakten/ZahlenFakten-2015.pdf

[2] Bund Ökologische Lebensmittelwirtschaft, Nachhaltige Verpackung von Bio-Lebensmitteln. Ein Leitfaden für Unternehmen, (2011) [cited 2016-02-14]
URL
http://herbaria.com/downloads/BOELW_Verpackungsleitfaden.pdf#page=41

[3] R. Coles, M. Kirwan, Food and beverage packaging technology, 2nd Edition, Chichester, Ames: Wiley-Blackwell, 2011, p. 101.

[4] B. Steward, Verpackungsdesign, 1st Edition, London: Stiebner Verlag GmbH, 2008, p. 173.

[5] H. Martin, Transport- und Lagerlogistik: Planung, Struktur, Steuerung und Kosten von Systemen der Intralogistik, 9th Edition, Hamburg: Springer Verlag, 2014, pp. 78-85.

[6]   P. Böröcz, Measurement and Analysis of Deformation Shapes on Corrugated Cardboard Logistical Boxes Under Static and Dynamic Compression, Acta Technica Jaurinensis 8 (4) (2015) pp. 320-329.
doi: 10.14513/actatechjaur.v8.n4.389

[7]   V. Köstner, J. B. Ressel, B. Sadlowsky, P. Böröcz, Individual Test Rig for Measuring the Creep Behaviour of Corrugated Board for Packaging, Acta Technica Jaurinensis 10 (2) (2017) pp. 148-156.
doi: 10.14513/actatechjaur.v10.n2.445

[8]   J-W. Rhim, Effect of Moisture Content on Tensile Properties of Paper-based Food Packaging Materials, Food Science and Biotechnology 19 (1) (2010) pp. 243-247.
doi: 10.1007/s10068-010-0034-x

[9]   V. Chonhenchob, S. P. Singh, Testing and Comparison of Various Packages for Mango Distribution. Journal of Testing and Evaluation 32 (1) (2004) pp. 69-72.
doi: 10.1520/JTE11888

[10] V. Chonhenchob, S. P. Singh, A Comparison of Corrugated Boxes and Reusable Plastic Containers for Mango Distribution, Packaging Technology and Science l6 (6) (2003) pp. 231-237.
doi: 10.1002/pts.630

[11] K. Saha, S. P. Singh, J. Singh, Sensory Evaluation of Fresh Cut Mangos Packaged in Rigid Containers Subjected to Mechanical Abuse by Transport Vibration, Journal of Applied Packaging Research 5 (3) (2011) pp. 181-195.

[12] Gesamtverband der Deutschen Versicherungswirtschaft e. V. (GDV), Mangoes, GDV (2016) [cited 2016-02-22]
URL http://www.tis-gdv.de/tis/ware/obst/mango/mango.htm

[13] Verband der Automobilindustrie, Standardisierte Einwegverpackungen für Seecontainer-Anwendungen, VDA 4525 (2009)